1   # Identification of the <u>Occurrence</u> of Minor Elements in the Structure of

2   # Diatomaceous Opal Using FIB and TEM-EDS

3   # (Revision 1)

4   Peng Yuan[1,2]*, Dong Liu[1,2], Junming Zhou[1,2], Qian Tian[1,2], Yaran Song[1,2], Huihuang Wei[1,2], Shun

5   Wang[1,2], Jieyu Zhou[1,2], Liangliang Deng[1,2], Peixin Du[1,2]

6

7   [1]*CAS Key Laboratory of Mineralogy and Metallogeny/Guangdong Provincial Key Laboratory of*

8   *Mineral Physics and Materials, Guangzhou Institute of Geochemistry, Institutions of Earth Science,*

9   *Chinese Academy of Sciences, Guangzhou 510640, China*

10   [2]*University of Chinese Academy of Sciences, Beijing 100049, China.*

11

12

13   *Corresponding author:

14   Prof. Dr. Peng YUAN

15   CAS Key Laboratory of Mineralogy and Metallogeny, Guangzhou Institute of

16   Geochemistry, Chinese Academy of Sciences (CAS)

17   Wushan, Guangzhou 510640, China

18   Tel/Fax: +86 20 85290341

19   E–mail address: (yuanpeng@gig.ac.cn)

20

Abstract

21

22   The occurrence of minor elements in the structure of biogenic diatomaceous opal-A

23   is an important issue because it is closely related to some bio-geochemical processes

24   driven by the precipitation, sedimentation and storage of diatoms, as well as to the

25   properties and applications of diatomite, the sedimentary rock composed of diatomaceous

26   opal-A. However, to date, there is no direct microscopic evidence for the existence of

27   minor elements, such as Al, Fe, and Mg, in the structure of diatomaceous opal-A, because

28   such evidence requires observation of the internal structure of frustules to exclude the

29   disturbance of impurity minerals, which is technically challenging using conventional

30   techniques. In this work, transmission electron microscopy (TEM) and scanning electron

31   microscopy (SEM) combined with energy-dispersive X-ray spectroscopy (EDS) mapping

32   analysis were performed on diatomaceous opal-A from three typical diatomite specimens

33   that were pretreated using focused ion beam (FIB) thinning. This technique produces a

34   slice of a diatom frustule for direct TEM observation of the internal structure of the

35   diatomaceous opal-A. The results of this work clearly indicate that minor elements, such

36   as Al, Fe, Ca, and Mg, conclusively exist within the siliceous framework of diatomaceous

37   opal-A. The contents of these minor elements are at atomic ratio levels of 1 (minor

38   element) / 10000 (Si) – 1/100, regardless of the genus of the diatoms. The occurrence of

39   minor elements in the internal structure is likely through biological uptake during

40   biosynthesis by living diatoms. Moreover, surface coatings composed of aluminosilicates

41   on diatom frustules are common, and the contents of elements such as Al and Fe are tens

42   or hundreds of times higher in the coatings than in the internal siliceous structure of

43   diatomaceous opal-A. The discovery of the incorporation of the abovementioned minor

44   elements in the diatomaceous opal-A structure, both in the internal Si-O framework and

45   on the surface, updates the knowledge about the properties of diatomite.

46   **Key words:** Diatomaceous opal-A; Diatomite; Focused ion beam (FIB); Transmission

47   electron microscopy (TEM); Minor elements.

Introduction

48

49   Opal is a naturally occurring hydrous silica mineral that forms in a variety of surface

50 and near-surface low-temperature environments (Webb and Finlayson 1987; Guthrie et al.

51 1995). According to its different structural states, opal has been divided into three groups,

52 i.e., opal-A, opal-C, and opal-CT, where A, C, and T signify amorphous, cristobalite, and

53 tridymite, respectively (Jones and Segnit 1971; Guthrie et al. 1995). Biogenic opal-A is a

54 widely occurring form of natural opal and is produced from the mineralization of some

55 common Si-bearing organisms, such as diatoms and sponges (Shi et al. 2012;

56 Wysokowski et al. 2018), which are ubiquitous in many ancient and modern marine and

57 lacustrine environments. Over the past few decades, biogenic opal-A has received

58 considerable research attention due to its essential role in some key geochemical

59 processes, such as the global biogeochemical cycle and related atmospheric carbon

60 fixation (Treguer et al. 2018).

61   Diatomaceous opal is the most investigated type of biogenic opal-A. It is sourced

62 from single-cell algae known as diatoms. Diatoms account for ~40% of oceanic primary

63 production on Earth and control the biogenic cycling of silicon (Si) throughout the

64 world's oceans (Treguer and De La Rocha 2013; Conley and Carey 2015). The inorganic

65 part of a diatom frustule is composed of amorphous silica, which builds up diatomaceous

66 opal-A in the postmortem stage of diatoms. Over geological time, the deposition of the

67 frustules of dead diatoms at the bottom of oceans and lakes results in a huge

68 accumulation of diatomaceous opal-A after a diagenesis process. The role of

69 diatomaceous opal-A as a Si sink, as well as the close relation of diatomaceous opal-A

70 with geochemical processes driven by diatoms, have attracted great research interest

71 (Michalopoulos and Aller 1995; De La Rocha et al. 1998; Presti and Michalopoulos

72 2008). Additionally, sedimentary rocks rich in diatomaceous opal-A have also received

73 much research attention because such rocks exhibit high porosities sourced from the

74 original porosity of the diatom frustules, making them excellent hydrocarbon reservoirs

75   (Cortese et al. 2004; Shukla and Mohan 2012).

76   Moreover, diatomite (also known as diatomaceous earth or kieselgur), the

77   sedimentary rock composed of diatomaceous opal-A and minor impurities such as clay

78   minerals, is the result of the accumulation and compaction of fossilized remains of

79   diatoms over geological time and is widely used in a variety of applications in industry,

80   such as filter, catalytic support, filler, absorbent, and biomedical materials (Yuan et al.

81   2004; Losic et al. 2009; Jin et al. 2014; Maher et al. 2018). Such extensive industrial

82   applications of diatomite are attributed to the intricate and porous frustule structure and

83   the desirable physical and chemical properties of diatomaceous opal-A, such as strong

84   absorptivity, low density, low thermal conductivity, high melting point and chemical

85   inertness (Yuan et al. 2004).

86   In the structure of opal-A minerals, the occurrence of minor elements, i.e., those

87   other than Si, O and H, may be very important in terms of its properties and sometimes

88   for its applications. In some studies (Gaillou et al. 2008), the non-Si elements (such as Al,

89   Fe, Ca, K, and Mg) present at concentrations above 500 ppm in nonbiogenic opal

90   minerals have been defined as "impurities", and the non-Si elements (such as Ba, Sr, Rb,

91   Mn, and Ti) at concentrations below 500 ppm have been termed "trace elements".

92   However, to simplify the description, the present paper uses "minor elements" to refer to

93   both impurity elements and trace elements. The occurrence of minor elements in the

94   structure of opal minerals directly affects their property, color, and appearance, such as

95   the body color of gem opals (Gaillou et al. 2008; Martin and Gaillou 2018). Many

96   previous studies have investigated the formation mechanisms of nonbiogenic

97   low-temperature opal minerals and the possible mechanisms regarding the occurrence of

98   minor elements in the structure of gem opal (Bartoli et al. 1990; Brown et al. 2004;

99   Chauvire et al. 2019; Horton et al. 2002; Gaillou et al. 2008).

100   For biogenic diatomaceous opal-A, the presence of minor elements in its structure is

101   an issue with particular importance. The minor elements in diatomaceous opal-A are

102   closely related to some bio-geochemical processes, such as CO_2 immobilization and

103   organic preservation, which are driven by the sedimentation and storage of diatoms and

104   constitute a key part of oceanic biological pump (Treguer and De La Rocha 2013). For

105   example, Al is the most investigated element that has been considered to be possibly

106   incorporated into the frustules of diatoms both in natural marine environments and under

107   cultured conditions (Moran and Moore 1988; Gehlen et al. 2002). Cocycling of Si and Al

108   based on the intake of Al by diatoms in the ocean has thus been proposed. Furthermore,

109   Al incorporation into frustules was found to have significant effects on lowering the

110   dissolution of frustules in the marine water column (Dixit et al. 2001). Therefore, the

111   amount of biogenic Si transferred through the water column and accumulated in abyssal

112   sediments is increased because of Al incorporation. This relationship is essential for the

113   delivery of the organics in diatoms from the water column to the deep-sea or the seafloor

114   and is therefore important for the preservation of organics via the deposition of frustules

115   (Treguer et al. 2018).

116   Although Al incorporation into the structure of diatoms has been documented based

117   on observations of natural and cultured diatoms (Koning et al. 2007), identification of the

118   exact state of the Al in the diatom structure has not been achieved. Particularly, the issue

119   of whether Al exists in the structure of the inorganic siliceous component, i.e., the

120   diatomaceous opal-A, remains ambiguous. From the perspective of mineral chemistry,

121   the significance of this issue lies in that it is an important factor affecting the property of

122   diatomaceous opal-A, and it also influences the stability of Al in diatom frustules and is

123   thus closely related to the Al cycle in the oceanic environment (Gehlen et al. 2003; van

124   Hulten et al. 2014; Moran and Moore 1988).

125   However, the detection of Al occurrence in the structure of diatomaceous opal-A is

126   technically challenging. The major difficulty is that tiny (micron dimension) impurities of

127   clay mineral particles are always associated with diatoms in natural environments, so

128   selective detection of the signal of Al occurrence inside the bulk diatoms is quite difficult.

129   As noted by Gehlen et al. (2002), for the structural and compositional characterization of

130   diatom frustules, the disturbance from impurities, such as the clay component in frustule

131   (e.g., in the pores), cannot be excluded even when the greatest care was taken to avoid

132   such contamination. Studies on the purification of diatomite ore have also demonstrated

133   that the association between clay impurities and diatom frustules is too close to

134   effectively remove impurities without disturbing the frustules (Ibrahim and Selim 2010;

135   Loucaides et al. 2012). Consequently, there is to date no conclusive evidence (such as

136   that from microscopic observation) for the existence of Al in the structure of

137   diatomaceous opal-A, despite some X-ray absorption spectroscopy studies suggesting

138   that tetrahedral Al exists inside the silica framework of diatoms (Gehlen et al. 2002;

139   Koning et al. 2007). Obviously, a study focused on microscopic evidence needs to be

140   conducted to directly determine whether Al exists in the internal structure of the siliceous

141   structure of diatomaceous opal-A. Compared with Al, the occurrence of other minor

142   elements, such as Fe, Mg, Ca, K and Zn, in diatom frustules has received much less

143   research attention (de Jonge et al. 2010; Ingall et al. 2013). Therefore, it is very necessary

144   to conduct a direct identification of the occurrence of all the above-mentioned minor

145   elements in the structure of diatomaceous opal-A.

146   In this work, the occurrence and features of minor elements (such as Al, Fe, Mg, and

147   Ca) in the structure of diatomaceous opal-A were examined using transmission electron

148   microscopy (TEM) and scanning electron microscopy (SEM) combined with

149   energy-dispersive X-ray spectroscopy (EDS) mapping analysis. The diatom frustules

150   were sliced using focused ion beam (FIB) thinning, which allowed direct electron

151   microscopy characterization of the internal siliceous structure of the diatomaceous opal-A.

152   This technique effectively avoids the possible interference of the impurity phase (such as

153   clay or iron oxide minerals) closely associated with diatomaceous opal-A. By applying

154   the above-mentioned characterizations, this work identifies the occurrence of the minor

155   elements in the internal structure of diatomaceous opal-A for the first time. Based on the

156   obtained results, some updates of the understanding of the structure and property of

157   diatomaceous opal-A are proposed, and some related implications are discussed.

158

Samples and Methods

160   **Diatomite samples**

161   Three diatomite samples from China, Australia, and USA were used in this study.

162   The Chinese diatomite sample was collected from the diatomite mine in Changbai County,

163   Jilin Province, with the genus *Coscinodiscus Ehrenberg* (Centrales) as the dominant

164   diatom species. This sample is denoted C-Dt hereafter. The Australian diatomite sample

165   (denoted S-Dt) is from the Mount Sylvia diatomite mine in south Gatton in southeastern

166   Queensland, with the genus *Melosira granulate* (Ehr.) *Ralfs* (Centrales) as the dominant

167   diatom. The American diatomite (denoted L-Dt) is from the Lompoc diatomite mine in

168   Santa Barbara county, southwestern California. L-Dt contains several major diatom

169   species, such as *Thalassiothrix longissima* Cleve *et* Grunow, *Coscinodiscus radiates*

170   Ehrenberg*, Coscinodiscus curvatulus* Grunow, and *Actinocyclus cholnokyi* Van

171   Landingham. The diatom of the genus *Thalassiothrix longissima* Cleve *et* Grunow

172   (Pennales) was used in this study. The selection of these representative diatomite samples

173   is based on consideration on the genus of the diatoms and the mine itself. L-Dt originates

174   from oceanic diatoms; bot C-Dt and S-Dt are from freshwater diatoms. The diatomite

175   mine where L-Dt was collected is among the largest oceanic diatomite mines in the world,

176   and the diatomite mine where C-Dt was collected is the largest one in China.

177

178   **Characterization methods**

179   The powder X-ray diffraction (XRD) patterns of the diatomite samples were taken

180   on a Bruker D8 Advance diffractometer with Ni filter and CuK$_\alpha$ radiation ($\lambda = 0.154$ nm)

181   using a generator voltage of 40 kV, a generator current of 40 mA, and a scan rate of 1°

182   (2θ)/min. The contents of major elements were determined by X-ray fluorescence

183   spectrometry (XRF) using an XRF-1800 wavelength dispersive sequential scanning

184   spectrometer (Shimadzu Corporation, Japan) with a voltage of 40 kV and current of 70

185   mA.

186   FIB thinning was carried out using a FIB-SEM (FEI Helios NanoLab 450S)

187   equipped with a FlipStage and *in situ* scanning TEM (STEM) detector, a Tomahawk ion

188   column, and a multichannel gas injection system. The diatom frustules for

189   characterization were picked from the diatomite powder using a nanomanipulator

190   (Oxford OmniProbe 200) and were then transferred to the copper specimen stage. For

191   FIB milling to obtain a thin slice of the frustule, a 5 kV focused gallium ion (Ga^+) beam

192   with a beam current of 40 pA was used, and the total thinning time was 2 min. Fig. 1

193   schematically presents the process of the FIB slicing of both sides and example images of

194   the FIB treatment on a *Melosira granulate* (Ehr.) *Ralfs* (Centrales) diatom from S-Dt. The

195   thickness of the obtained frustule slice is approximately 40 nm. The slice was then fixed

196   on the edge of FIB half grid that is made of molybdenum (Mo) by induced platinum (Pt)

197   deposition.

198

199   **Figure 1**

200

201   The *in situ* field emission SEM (FE-SEM) observation of the frustule slice was

202   performed with an accelerating voltage of 30 kV and a current of 24 - 9300 pA. Before

203   FE-SEM observation, the sputtering of chromium (Cr) was carried out to make an

204   ultra-thin electrically-conducting coating. The elemental distribution of the sliced frustule

205   was obtained using energy-dispersive X-ray imaging attached to a transmission electron

206   microscope (FEI Talos F200 TEM/EDS microscope) with a voltage of 200 kV and a

207   current of 1 nA. The limit of detection of the EDS accessory (FEI Super-X EDS) is

208   0.01wt% and the accuracy of quantification is over 0.1wt%. The spatial resolution of

209   EDS analysis is lower than 5 nm.

210   The raw EDS data of the weight percentage (wt%) of the elements were obtained.

211 And they were transformed to the relative atomic concentration of the elements (to Si

212 atomic concentration), as a normalization that excludes the influence of nonindigenous

213 elements such as Ga, Mo and Pt. Notably, the signal of Na is strongly disturbed by the

214 signal of the Ga from the FIB treatment, so its EDS data were not reported.

215

216   **Results**

217 **Mineralogical composition of the diatomite samples**

218   The XRD patterns (Fig. 2) show that amorphous opal-A is the main mineral

219 component of all diatomite samples, as evidenced by the broad diffraction pattern

220 centered at approximately $21°(2\theta)$. Quartz is found in all diatomite samples, but

221 cristobalite only exists in L-Dt (Fig. 2). Additional weak peaks are observed at

222 approximately $7°(2\theta)$ and $9°(2\theta)$ for C-Dt (Fig. 2a), and $13°(2\theta)$ for S-Dt (Fig. 2b). These

223 diffractions correspond to clay minerals, such as illite or kaolinite, indicating the

224 existence of a small amount of clay minerals in C-Dt and S-Dt.

225   The chemical compositions of C-Dt, S-Dt, and L-Dt are as follows. C-Dt: SiO_2,

226 78.22%, Al_2O_3, 7.86%, Fe_2O_3, 3.02%, CaO, 0.46%, MgO, 0.67%, K_2O, 0.79%, Na_2O,

227 0.41%, TiO_2, 0.23%, and L.O.I, 8.04%; S-Dt: SiO_2, 86.48%, Al_2O_3, 3.56%, Fe_2O_3, 1.16%,

228 CaO, 0.52%, MgO, 0.69%, K_2O, 1.03%, Na_2O, 0.34%, TiO_2, 0.22%, and L.O.I, 6.55%;

229 and L-Dt: SiO_2, 84.65%, Al_2O_3, 5.72%, Fe_2O_3, 1.27%, CaO, 0.32%, MgO, 0.41%, K_2O,

230 0.10%, Na_2O, 0.19%, TiO_2, 0.25%, and L.O.I, 7.20%.

231

232   **Figure 2**

233 **Morphology and overall elemental distribution features of diatom frustules**

234   The FE-SEM and TEM images of the diatom frustules from the three original

235   diatomite specimens, C-Dt, S-Dt, and L-Dt, are shown in Figs. 3-8. Fig. 3a shows a

236   frustule with the typical morphology of diatom of the genus *Coscinodiscus* Ehrenberg in

237   C-Dt. Like well documented in previous studies (Liu et al. 2010, 2012; Wang et al. 2013),

238   the frustules of this diatom genus have a disk shape (in plan view) and a round

239   soapbox-like structure, of which the porosity is high. As measured in our previous study

240   (Liu et al. 2010), the frustules in C-Dt are relatively uniform in diameter (20-40 μm) and

241   thickness (1.2-1.8 μm). The pores at the edge region of the frustules form an ordered

242   hexagonal array and have diameters of 100-250 nm, whereas the pores in the central

243   region of the frustule (Fig. 3a, the inset at right corner) have diameters of 300-800 nm. A

244   fragment of the upper epivalve (Fig. 3b) with a length of approximately 35 μm (Fig. 3c),

245   obtained from FIB thinning, was used for further TEM characterization (Fig. 4).

246   Two rectangular areas (Area-A and Area-B, indicated in Fig. 3c) on the sliced

247   fragment of frustule were selected for EDS mapping scanning analysis. Area-A (Fig. 3c)

248   is an area that contains both an external surface and a sliced internal surface of the

249   frustule, and Area-B (Fig. 3c) is a zone within the newly exposed surface of the sliced

250   fragment after FIB treatment. Fig. 3d displays the EDS mapping images of Area-A. The

251   Si distribution in this area clearly displays the siliceous opal-A structure of the frustule.

252   Minor elements, such as Al, Fe (Fig. 3d), Mg, Ca, and K (images not shown; results

253   shown in Table 1) are also observed in the siliceous structure of the frustule. The

254   distribution of these minor elements is not homogeneous, and a variation in the

255   concentration of the elements in different regions is exhibited (Fig. 3d). The content of

256   minor elements in Area-A is higher than those in Area-B (Table 1). For example, the

257   average Al/Si and Fe/Si atomic ratios (shorted as Al/Si and Fe/Si ratios hereafter) of

258   Area-A is 0.0230 and 0.0047, whereas the Al/Si and Fe/Si ratio of Area-B is 0.0052 and

259   0.0017, respectively. These results indicate that the minor elements are more concentrated

260   in the surface area than in the internal structure. Consequently, EDS mapping analysis at

261   higher resolution is necessary to reveal the elemental distribution in different locations in

262   the detailed microstructure of the frustule.

263

264   **Figure 3**

265

266   Fig. 4a shows the TEM image of a further sliced fragment in the fragment shown in

267   Fig. 3c. As detailed in Fig. 4b, eight different places in the fragment were selected for

268   EDS mapping. The resulting elemental distribution results, represented by their atomic

269   ratios to Si, are listed in Table 1. The elemental distribution results of analogous places at

270   other frustules (images not shown) in the same diatomite sample are also summarized in

271   Table 1.

272

273   **Figure 4**

274

275   As shown in Fig. 1a, the frustules of the diatoms of the genus *Melosira granulate*

276   (Ehr.) *Ralfs* in S-Dt have a typical tube-like structure. As indicated by TEM

277   measurements, most frustules have an external diameter of 10-16 μm and a thickness of

278   6-8 μm. The size of the pores in the tube wall of the frustules is 0.3-0.5 μm. A sliced

279   fragment (Fig. 1 and Fig. 5a) of the selected frustule is used for detailed TEM and EDS

280   mapping characterization.

281   Fig. 5b and 5c show the EDS mapping images of two selected areas (Area-I and

282   Area-II, indicated in Fig. 5a) in the sliced fragment. Area-I is an eyeglasses-like zone in

283   the wall of the frustule (Fig. 5b), and the "lens" of the zone has dimensions of

284   approximately 700 nm (length) × 500 nm (height). The Si concentration in the lens-like

285   zone is higher than any other region of Area-I, indicating a typical silica composition.

286   Area-II is another area of the frustule wall, and it also shows a siliceous composition in

287   the internal region (Fig. 5c). The average Al/Si ratios of Area-I and Area-II are 0.0047

288   and 0.0035, respectively. In both areas, as clearly evidenced by the EDS mapping results,

11

289   minor elements such as Al and Fe are present at higher concentrations at the surface or in

290   the near-surface region (referred to as "subsurface" hereafter) than in the internal region

291   (Fig. 5b and 5c), which is in line with the C-Dt observations.

292

293   **Figure 5**

294

295   Based on these observations, the minor elements in S-Dt frustule also show a

296   nonhomogeneous distribution: the minor elements such as Al, Fe, Mg, Ca, K, and Zn

297   have higher concentrations at the surface of the frustule than in the internal siliceous

298   structure (Table 1). This feature of the minor element distribution is similar to what was

299   observed for C-Dt.

300   Fig. 6a shows the TEM image of the further sliced fragment of the frustule shown in

301   Fig. 5. Fig. 6b and 6c show the TEM images of the left and right zones of the fragment,

302   respectively, at a high resolution. Eleven different places in the fragment (Fig. 6b and 6c)

303   were selected for in-depth EDS mapping. The corresponding elemental distribution

304   results are summarized in Table 1. In agreement with the abovementioned EDS mapping

305   analysis with a relatively large field of view (Fig. 5), the minor elements are more

306   concentrated in the surface or subsurface areas than in the internal structure. For example,

307   the average Al/Si ratios in the subsurface places (0.0852 for Place-1 and 0.0708 for

308   Place-7) are higher than those in the internal regions (0.0012 for Place-3 and 0.0016 for

309   Place-9) (Fig. 6 and Table 1), and the Al/Si atomic ratios in the internal structure are in

310   the range of 0.0009–0.0041.

311   **Figure 6**

312

313   As shown in Fig. 7a, the frustule of the diatom of the genus *Thalassiothrix*

314   *longissima* from L-Dt has a rod-like morphology, and the inside of the frustule has a

315   porous structure. Most frustules of such type have a length of 80-100 μm and an external

316   diameter of 3-5 μm. A frustule was first cut by FIB slicing into two halves along the

317   longitudinal axis direction, and a fragment (Fig. 7b) from one half was further sliced to

318   obtain a thin section (Fig. 7c) for TEM characterization. A rectangular area (marked in

319   Fig. 7c) was selected for EDS mapping, and the obtained images are shown in Fig. 7d. As

320   indicated by the images (Fig. 7d), the contents of Al and Fe at the surface is higher than

321   that in the internal siliceous wall of the frustule, whereas Si shows a homogenous

322   distribution throughout the frustule. Ten locations in the fragment (Fig. 7e) were selected

323   for further EDS mapping characterization at high resolution. The results of the elemental

324   distribution are summarized in Table 1.

325

326   **Figure 7**

327

328   **Elemental distribution in the internal siliceous structure of frustule**

329   Based on the contents of the minor elements of different diatomite samples (Table 1),

330   it is clear that minor elements occur in the internal structure of all samples of

331   diatomaceous opal-A. The average Al/Si ratios, in the internal structure of C-Dt, S-Dt,

332   and L-Dt, calculated from all obtained data of each diatomite, are 0.0040(22), 0.0021(10),

333   and 0.0026(16); and the average Fe/Si ratios are 0.0031(18), 0.0010(2), and 0.0006(3)

334   respectively. Overall, the contents of Al in the internal structure of all diatomaceous

335   opal-A are at the same order of magnitude, as they remain at atomic ratio levels of 1/1000

336   – 1/100 (Al/Si; Table 1). Despite that, variation of the contents of Al among different

337   places and different diatomaceous opal samples are obvious. The contents of Fe in the

338   internal structure of all diatomaceous opal samples are also at the same order of

339   magnitude with atomic ratio levels of 1/1000 – 1/100 (Fe/Si; Table 1). However, the

340   variation of Fe/Si ratios among different samples is slightly more pronounced than that of

341   Al/Si; for example, the Fe content in the internal structure of the diatomaceous opal from

342   L-Dt are lower than those for C-Dt and S-Dt (Table 1).

343   Mg, Ca, K, and Zn also occur in the internal structure of the diatomaceous opal-A,

344   but their contents are lower than those of Al and Fe. Generally, the contents of these

345   elements in the internal structure are at atomic ratio levels of 1 (minor element) /10000

346   (Si) – 1/100 (Table 1), and the average ratios for each sample are as follows. C-Dt: Mg/Si

347   (0.0027(16)); Ca/Si (0.0014(9)); K/Si (0.0020(14)); Zn/Si (0.0013(8)). S-Dt: Mg/Si

348   (0.0019(8)); Ca/Si (0.0007(5)); K/Si (0.0006(4)); Zn/Si (0.0005(3)). L-Dt: Mg/Si

349   (0.0014(2)); Ca/Si (0.0005(2)); K/Si (0.0006); Zn/Si (0.0004(2)). Similar to the

350   abovementioned results of Al/Si and Fe/Si, a variation in the contents of the minor

351   elements is shown among different sample. In general, the minor element contents in the

352   internal structure of the diatomaceous opal-A follows an order C-Dt > S-Dt > L-Dt

353   (Table 1).

Minor elements occurring in the surface or subsurface areas of frustule

355   As shown by the images with relatively large fields of view of the frustules (Fig. 3, 5,

356   and 7), the contents of minor elements at the surface area of the frustule are higher than

357   that in the internal siliceous structure. In the high-resolution EDS mapping images,

358   enrichment of minor elements, such as Al and Fe, at the surface is frequently observed.

359   Notably, in some surface locations (such as the place outlined by dashed square in the

360   right corner of Fig. 4b), high Ga and Pt concentrations are observed. These signals

361   mainly resulted from the contamination by FIB pretreatment.

362   One major example of the minor elements enrichment at surface is the coating of

363   impurity minerals on the surface of the frustules, where the minor elements are the

364   chemical constituents of the coating minerals. As exemplified by the area shown in Fig.

365   8a, a layer of coating (with a thickness of approximately 57-70 nm) on the inner surface

366   of the pores (Place-1, Fig. 4b and 8a) in the frustule from C-Dt is clearly resolved. In the

367   high-resolution observations, the layer-related domain exhibits a one-dimensional lattice

368   fringe of clay minerals and shows a *d*-spacing of approximately 1.0 nm (Fig. 8b, the inset

369   on the right bottom). This value is in good agreement with the d_{001} value calculated from

370   the selected area electron diffraction (SAED) pattern (Fig. 8b, the inset on the left

371   bottom). These results indicate that the minerals attached to the surface of the diatomite

372   might be illite or muscovite. Notably, the EDS analysis of abovementioned area (Place-1)

373   shows that the Al/Si ratio of the area is 0.3907 (Table 1), which is much lower than the

374   ideal Al/Si ratio of illite. The reason might be that the signal from the internal siliceous

375   structure was also included in the EDS signal of the mentioned area (Place-1 in Fig. 4b).

376

377   **Figure 8**

378

379   In another major example of the surface enrichment of the minor elements

380   (exemplified by Place-6 shown in Fig. 4b and Fig. 8c), the component of the surface

381   coating is fine-grained clay minerals; instead, the coating is composed of Al (or Fe)-rich

382   poorly crystalline components (Fig. 8c). The amorphous nature is indicated by the broad

383   and isotropic halo SAED pattern (Fig. 8d, the inset). The Al/Si and Fe/Si ratios of the

384   amorphous phase are 0.4777 and 0.1403, respectively, which are similar to the Al/Si and

385   Fe/Al ratios of the composition of some natural iron-containing aluminosilicates. Notably,

386   thin coatings of clay minerals or poorly crystalline Al-rich phases are readily observed on

387   the surfaces of frustules from different diatomite samples by using conventional TEM

388   characterization (without FIB pretreatment), suggesting the common existence of the

389   coating of Al-rich phases.

390   In addition to the surface coating, the minor element enrichment in the subsurface

391   areas is also observed. Table 1 shows that the Al/Si ratios in the subsurface locations are

392   much higher than that in the internal siliceous structure, e.g., Place-3, Place-4, and

393   Place-7 for C-Dt (Fig. 4b, Table 1); Place-1, Place-4, Place-7 and Place-10 for S-Dt (Fig.

394   6b and 6c, Table 1); Place-4, Place-5, and Place-9 for L-Dt (Fig. 7, Table 1). These

395   subsurface areas are within the near-surface zone with depth of up to approximately 80

396 nm, and the minor element contents (exemplified by Al/Si ratio) of these areas are at a

397 range 0.01-0.09, which are tens of times greater than those of the internal structure

398 (detailed in Table 1). However, such Al/Si ratios are ten times lower than the Al/Si ratio

399 of the abovementioned clay-like coating (Table 1). In addition, the bulk phase of such

400 relatively Al-rich regions in the subsurface areas is still amorphous silica, indicated by the

401 broad halo-like SAED pattern (not shown).

402

403 # Discussion

404 **Forms of the minor elements occurring of in diatomite frustules and their effects on**

405 **the properties of diatomaceous opal-A**

406   Previously, the structural incorporation of Al into the structure of diatom frustules

407 was proposed based on spectroscopic characterization using Al K-edge X-ray absorption

408 near edge structure (XANES) spectroscopy (Gehlen et al. 2002). Tetrahedral Al exists

409 inside the silica framework of diatoms through Al-Si substitution has been suggested

410 based on the above-mentioned spectroscopic studies. However, direct evidence of the Al

411 occurrence inside the siliceous structure of diatomaceous opal has not been obtained, due

412 to the disturbance of impurity minerals can not be excluded (Gehlen et al. 2002; Koning

413 et al. 2007). For the first time, the present work provides a direct microscopic evidence of

414 the occurrence of minor elements in the structure of diatomaceous opal-A, as clearly

415 shown by the EDS elemental mapping results of the internal structure of the

416 diatomaceous opal-A.

417   The minor element occurrence in the internal siliceous structure indicates that the

418 incorporation of these elements occurred through biological uptake during the

419 biosynthesis of living diatoms because the incorporation of elements (such as Al) into

420 diatom frustules in the post-mortem stage of diatoms mainly occurred at the surface of

421 the frustules (Koning et al. 2007). Specifically, in incubation experiments in which

422 diatoms were cultured in seawater at varying Al concentrations (2 to 500 nM) for periods

16

423 of up to 6 months, Koning et al. (2007) found the formation of an aluminum-rich silicate

424 phase on the surface of the diatom frustules, which indicated the rapid postmortem uptake

425 of aluminum by the diatom frustules. The precipitation of this surface phase occurs under

426 experimental conditions mimicking those prevailing at the sediment–water interface

427 (Koning et al. 2007). Thus, the results of that study effectively support the

428 postdepositional uptake of Al by diatom frustules during early diagenesis (Dixit et al.

429 2001). Furthermore, the results suggest that the occurrence of Al incorporation in the

430 internal structure of diatomaceous opal-A is unlikely to occur as a postdepositional

431 process. This perspective is also supported by the study conducted by Houston et al.

432 (2008), in which the surface precipitation of aluminum hydroxides and aluminosilicate

433 solids was regarded to occur on the surface of amorphous silica, based on bulk solution

434 chemistry measurements combined with solid-state nuclear magnetic resonance (NMR)

435 techniques.

436 Therefore, there exist two basic forms of incorporation of minor elements in

437 diatomaceous opal-A. One involves the incorporation of minor elements into the silicon

438 framework via biological uptake during biosynthesis by living diatoms. The content of

439 the minor elements of this type are at atomic ratio levels of 1 (minor element) / 1000 (Si)

440 or lower (Table 1). The other form occurs as a surface coating that very likely develops

441 through inorganic uptake during the postmortem alteration of the diatom frustule (Koning

442 et al. 2007). Elements such as Al and Fe occur in the form of surface Al (or Fe)-rich

443 silicate phases, and their contents are tens or hundreds of times higher than those in the

444 internal siliceous structure of diatomaceous opal-A.

445 There exist considerable uncertainty regarding the states of the minor elements in

446 the internal Si-O framework of diatomaceous opal-A as well as how they entered into the

447 siliceous framework. As mentioned above, it has been thought that the occurrence of Al

448 incorporation in the internal structure of diatomaceous opal-A unlikely occurs at a

449 postdepositional process (Dixit et al. 2001; Koning et al. 2007). In the meantime, it is

450 well known that Al is not a necessary nutrient for the growth of diatoms, and Al is also

451 not needed for the assembling of biosilica as building block for the construction of the

452 frustules during diatoms growth (Kröger et al. 1999). Despite that, the possibility that Al

453 could be unintendedly brought into the siliceous framework during the biosynthesis

454 process of living diatoms can not be excluded. That means the isomorphous Al-Si

455 substitution might occur at the growth of diatoms, such as the biologically-driven

456 assembling of biosilica, although more investigation on this subject is beyond the scope

457 of the present work.

458   Unlike Al, the other involved elements, such as Fe, Ca, Mg, K, and Zn, etc., are the

459 necessary nutrients for the growth of diatoms (Cooksey and Cooksey 1988; Ushizaka et

460 al. 2008; Armbrust 2009; Marchetti et al. 2009). So it is likely that their occurrence in the

461 internal siliceous structure of frustules has something to do with the biological uptake

462 during the biosynthesis of living diatoms. Theoretically, the isomorphous substitution of

463 Al and Fe in siliceous structure is able to produce local charge deficiency, which could be

464 subsequently compensated by the exchangeable K, Na, Ca, and Mg cations (Webb and

465 Finlayson 1987; Gehlen et al. 2002; Gaillou et al. 2008; Rondeau et al. 2012). However,

466 the exact mechanism, e.g., the timing of such charge compensation or the underlying

467 driving force that might be highly sensitive to the biosynthesis pathways, remains

468 unknown and needs further investigation. There is a notable difference in the contents of

469 the minor elements between biogenic diatomaceous opals and continental opals, e.g., the

470 gem opals reported by Gaillou et al. (2008). For example, the Zn abundance in

471 diatomaceous opal-A are considerably high (Table 1), whereas the Zn abundance are

472 normally very low in continental opals (Brown et al., 2004; Gaillou et al. 2008). In

473 addition, the Al concentrations in the subsurface places of diatomaceous opals are with

474 the same order of magnitude as that in continental opals, whereas the Al concentrations in

475 the internal structure of diatomaceous opals are much lower.

476   Furthermore, the Al and Fe concentrations in the different places of a diatom frustule

477   is not uniform (Table 1), even for the internal structure. Such variation of the elements

478   concentration in the same frustule reflects the inhomogeneous composition of the frustule,

479   which is affected by the diatom structure itself, as well as by the uptake of elements by

480   diatoms from their living environments. The Al concentration in lake and sea water could

481   vary in a short period (e.g., in one month) (Hydes, 1989; Koshikawa et al., 2002). This

482   result implies the elements uptake during the growth of diatoms might be changeable and

483   thereby might affect the chemical composition of diatomaceous opals. However, it is

484   unclear how the compositional variations of diatoms were influenced by the

485   biomineralization process during the growth of diatoms so no further discussion could be

486   made at this stage.

487   The elements on the surface of diatomaceous opal-A might be associated with the

488   formation of aluminosilicate, such as fine clay minerals, in which these elements act as

489   structural components. In addition, they could be adsorbed by the frustules through

490   electrostatic interactions (Gehlen et al. 2002). An interesting observation is that the minor

491   element content in the subsurface area (Table 1) is higher than that of the internal

492   structure but lower than that of the surface coating. This pattern might be a result of the

493   inward diffusion of the related elements from the surface.

494   Mineralogically, the identification of the incorporation of the abovementioned minor

495   elements in the diatomaceous opal-A structure, both in the internal Si-O framework and

496   at surface, is of significance for better understanding the structure and properties of

497   biogenic opal-A, as well as for updating the knowledge regarding the applications of

498   diatomite, in which diatomaceous opal-A acts as the dominant component. As a result of

499   the occurrence of tetrahedrally coordinated Al and Fe, AlOH and FeOH groups occur in

500   the siliceous structure of diatomaceous opal-A. This result implies that the types of

501   hydroxyl groups in the structure of diatomaceous opal-A are not limited to silanols

502   (SiOH), whose types have been well identified based on a comprehensive infrared

503   spectroscopy (Bobon et al. 2011; Chauvire et al. 2017; Yuan et al. 2004) and NMR (Yuan

19

504   et al. 2001) studies.

505   Particularly, even though the Al/Si or Fe/Si ratio in the internal siliceous structure of

506   diatomaceous opal-A is low (approximately 0.0009–0.0065 for Al/Si and 0.0003–0.0065

507   for Fe/Si, varying with different specimens), the Al/Si and Fe/Si ratios in the surface or

508   subsurface areas are tens or even hundreds times greater than the bulk Al/Si ratio (Table

509   1). Therefore, the hydroxyl groups associated with the minor elements in the surface area

510   play an important role in the reactivity of diatomaceous opal-A, and they should be taken

511   into account in the studies on the related interface reactions of diatomaceous opal-A.

512   Furthermore, the AlOH groups at substitution site in the siliceous structure of

513   diatomaceous opal-A likely have stronger Brønsted (B) acidity than the SiOH groups,

514   similar to the case of amorphous Si-Al oxides, as well documented previously (Niwa et al.

515   2010). Such AlOH groups readily transform to Lewis (L) acid sites after the

516   dehydroxylation resulting from the calcination treatment (Niwa et al. 2010; Liu et al.

517   2016). This finding implies that the inherent solid acidity of diatomaceous opal-A might

518   be stronger than previously supposed, which was based on the assumption that

519   diatomaceous opal-A is "pure" silica leading to the assumption that both the Lewis and

520   Brønsted acidities are weak (Yuan et al. 2004; Liu et al. 2010).

521   Compared with the effects of the minor elements in the internal structure, the

522   abovementioned Al accumulation on the surface of frustules resulting from the coating of

523   very thin layers of clay minerals or amorphous nanoparticles might exert stronger effects

524   on the properties of diatomaceous opal-A. The surface clay layer might provide Lewis

525   acid sites, thereby contributing to the entire L acidity of diatomite (Yuan et al. 2004).

526   Notably, the close association of the clay layers with the frustule substrate means that the

527   clay coating is very difficult to remove, especially for those treated with physical

528   purification techniques, such as the sedimentation method. Therefore, the reactivity of the

529   clay (or amorphous Al-Si oxide) layers on the frustules could be considered an inherent

530   property of the diatomaceous opal-A or diatomite.

531   Moreover, the existence of surface clay layers directly affects the surface charge

532   (e.g., the isoelectric point, pH_{IEP}) of diatomaceous opal-A. It is well documented that the

533   pH_{IEP} of pure silica is approximately 2.0 (Lazaro et al. 2018). However, the C-Dt sample

534   that was treated with only sedimentation purification shows a negative potential across

535   the whole pH range of determination, so the pH_{IEP} of the sample was not obtained (see

536   details from the Supporting Information). This result is due to the surface clay layers

537   being constantly negatively-charged (Bergaya et al. 2006), endowing the diatomite

538   frustules with a constant negative charge. In contrast, for the purified C-Dt that

539   underwent acid leaching and calcination treatment (see Supporting Information), a pH_{IEP}

540   of 1.9 was obtained. This finding is due to the removal of surface impurity minerals,

541   resulting in the recovery of the surface properties of amorphous silica. Therefore, great

542   care should be taken with the surface charge of diatomaceous opal-A, and the possible

543   effects of the surface Al (or Fe)-rich impurity layers must be considered.

544

545   **Implications**

546   The findings of this work answer the question "if the minor elements such as Al

547   exist in the internal structure of diatomaceous opal-A" that is of meaning for not only the

548   related geochemical processes but the applications of diatomite. The incorporation of the

549   minor elements into the structure of diatomaceous opal-A indicates that diatomaceous

550   opal-A acts as a considerable sink for these elements. The sedimentation and diagenesis

551   of diatoms in lake and ocean environments result in the stable preservation of

552   diatomaceous biogenic silica, and the global burial of such silica is substantial (Conley

553   and Carey 2015). The rate of burial of Si in the form of biogenic silica in the global

554   oceans is approximately 6.30×10^{12} mol per year (Treguer and De La Rocha 2013), and

555   that in the global lakes is approximately 1.30×10^{12} mol per year (Frings et al. 2014). As

556   documented in previous studies, the amounts of diatomaceous silica in the Lompoc

557   diatomite mine and Changbai diatomite mine reach up to approximately 8.0×10^{10} tons

558   (Snelling, 1995) and 2.5×10^8 tons (Zhang et al. 2019), respectively. Based on the

559   average atomic ratio of the minor elements in the internal structure for L-Dt and C-Dt, the

560   capacities of the sinks of the elements such as Al and Fe reach millions or even tens of

561   millions tons in these deposits. Therefore, the occurrence of minor elements in the

562   structure (or on the surface in the form of a thin coating) of diatomaceous opal-A in the

563   sedimentary rocks might be a non-negligible huge sink of these minor elements.

564   For oil and gas geology, sedimentary rocks rich in diatomaceous opal-A are regarded

565   as excellent hydrocarbon reservoirs (Montgomery and Morea 2001; Cortese et al. 2004)

566   because of their high porosity. The cation exchange capacity (CEC) is a very important

567   physicochemical property of sedimentary rocks because it is an indicator of the quantity

568   of hydrated cations (Derkowski et al. 2015), and is used also for various corrections and

569   calibrations in wireline log analysis during calculations on the porosity and permeability

570   in hydrocarbon reservoirs (Brown and Ransom 1996; Matteson et al. 2000; Derkowski et

571   al. 2015). The possible effects of the surface properties (such as CEC) of diatomaceous

572   opal on the petrophysical properties of the rock matrix in diatomaceous sedimentary

573   basins have been proposed recently (Derkowski et al. 2015). The present work specifies

574   that a variety of cations are incorporated in the diatom frustules and that fine-grained clay

575   layers occur on diatom frustules. This finding implies that the CEC value of the

576   diatomaceous opal-A in diatomaceous sedimentary rocks is very likely higher than the

577   theoretical CEC value of a pure opal, so considerable care should be taken for using the

578   CEC value of pure opal as reference data in the related calculation on the petrophysical

579   properties of diatomaceous sedimentary rocks. In addition, the changes in the surface

580   properties of the diatom frustules, induced by the minor elements, may affect other bulk

581   properties (such as the efficiency of oil recovery) of reservoirs in diatomaceous

582   sedimentary basins (Turov and Leboda 1999; Strand et al. 2007), and thereby should be

583   considered for such applications.

584   For the applications of diatomite, the meaning of the finding that minor elements

22

585   inherently exist in the siliceous structure of diatomaceous opal-A includes the following

586   aspects. On the one hand, this finding explains a phenomenon commonly reported in the

587   mine processing of diatomite, i.e., high-efficiency purification of diatomite is difficult to

588   achieve through physical purification (such as sedimentation or mild scrubbing

589   treatments) alone (Al-Wakeel 2009). As shown in Fig. 6, the nanoscale Al (or Fe)-rich

590   layer is too closely associated with the surface of diatom frustules to be removed by using

591   mild physical purification. Therefore, chemical purification, such as acid treatment,

592   seems to be a must-do method for obtaining high-purity diatomite products, despite that

593   acid leaching is not favorable because of the serious demand for lowering the

594   environmental impact of chemical purification technology. On the other hand, with the

595   knowledge that the diatomaceous opal-A in commercially available diatomite products

596   are actually not 'pure', the occurrence of the minor elements, especially in the form of

597   surface coatings on diatomaceous opal-A, must be considered in the applications of the

598   diatomite. For example, diatomite has been used as a catalytic support in industry for

599   loading active components, such as noble metals, and novel catalytic materials based on

600   diatomite are attracting increasing attention (Bahramian et al. 2008; Yuan et al. 2016).

601   Under such circumstances, much attention should be paid to either positive

602   catalysis-promoting effects or negative catalysis-dampening effects sourced from the

603   minor elements in diatomaceous opal-A.

604   Finally, simulating the formation of diatomaceous silica has attracted

605   multi-disciplinary research interest (Kröger and Poulsen 2008). The lessons and

606   inspirations from diatoms for developing novel nanotechnology (Losic et al. 2009), as

607   well as for biological materials science (Wysokowski et al. 2018), have been

608   comprehensively reviewed. The present finding concerning the minor elements in

609   diatomaceous opal-A suggests that the biomimetic synthesis based on diatoms is actually

610   mingled with the incorporation of non-silicon elements. Of particular interest is the

611   finding that the unnecessary element, such as Al, for the growth of diatoms, could be

612 incorporated into the internal siliceous structure of diatomaceous silica. To find ways

613 through biosynthesis to tailor the chemical composition and microstructure of

614 diatomaceous opal would be of significance for the development of next-generation

615 porous materials possessing intricate frustule-like structures and novel properties such as

616 catalytic activity. This subject is promising and deserves further study in the near future.

617

618 **Acknowledgements**

626

627

628

629

630

631

632

633

References Cited

Al-Wakeel, M.I. (2009) Characterization and process development of the Nile diatomaceous sediment. International Journal of Mineral Processing, 92, 128-136.

Armbrust, E.V. (2009) The life of diatoms in the world's oceans. Nature, 459, 185-192.

Bahramian, B., Ardejani, F.D., Mirkhani, V., and Badii, K. (2008) Diatomite-supported manganese Schiff base: An efficient catalyst for oxidation of hydrocarbons. Applied Catalysis A-General, 345, 97-103.

Bartoli, F., Bittencourt, R. D., Doirisse, M., Meyer, R., Philippy, R., Samama, J. C. (1990) Role of aluminium in the structure of Brazilian opals. European Journal of Mineralogy, 2, 611-619.

Bergaya, F., Theng, B.K.G., and Lagaly, G. (2006) Handbook of Clay Science, 876p. Kidlington, Oxford.

Bobon, M., Christy A.A., Kluvanec D., Illasova L. (2011) State of water molecules and silanol groups in opal minerals: a near infrared spectroscopic study of opals from Slovakia. Physics and Chemistry of Minerals, 38, 809-818.

Brown, K.M., and Ransom, B. (1996) Porosity corrections for smectite-rich sediments: Impact on studies of compaction, fluid generation, and tectonic history. Geology, 24, 843-846.

Brown, L.D., Ray, A.S., Thomas, P.S. (2004) Elemental analysis of Australian amorphous banded opals by laser-ablation ICP-MS. Neues Jahrbuch Mineral. Monatsh, 9, 411-424.

Chauvire, B., Rondeau, B., Alexandre, A., Chamard-Bois, S., La, C., Mazzero, F. (2019) Pedogenic origin of precious opals from Wegel Tena (Ethiopia): evidences from trace elements and oxygen isotope. Applied Geochemistry, 101, 127-139.

Chauvire B., Rondeau B., & Mangold N. (2017) Near infrared signature of opal and chalcedony as a proxy for their structure and formation conditions. European Journal of Mineralogy, 29, 409-421.

Conley, D.J., and Carey, J.C. (2015) Silica cycling over geologic time. Nature Geoscience, 8, 431-432.

Cooksey, B., and Cooksey, K.E. (1988) Chemical signal-response in diatoms of the genus amphora. Journal of Cell Science, 91, 523-529.

Cortese, G., Gersonde, R., Hillenbrand, C.D., and Kuhn, G. (2004) Opal sedimentation shifts in the

661   World Ocean over the last 15 Myr. Earth and Planetary Science Letters, 224, 509-527.

662   de Jonge, M. D., Holzner, C., Baines, S. B., Twining, B. S., Ignatyev, K., Diaz, J., Howard, D. L.,

663   Legnini, D., Miceli, A., McNulty, I., Jacobsen, C. J., Vogt, S. (2010) Quantitative 3D elemental

664   microtomography of Cyclotella meneghiniana at 400-nm resolution. Proceedings of the National

665   Academy of Sciences of the United States of America, 107, 15676-15680.

666   de La Rocha, C.L., Brzezinski, M.A., DeNiro, M.J., and Shemesh, A. (1998) Silicon-isotope

667   composition of diatoms as an indicator of past oceanic change. Nature, 395, 680-683.

668   Derkowski, A., Srodon, J., and McCarty, D.K. (2015) Cation exchange capacity and water content of

669   opal in sedimentary basins: Example from the Monterey Formation, California. American

670   Mineralogist, 100, 1244-1256.

671   Dixit, S., Van Cappellen, P., and Van Bennekom, A.J. (2001) Processes controlling solubility of

672   biogenic silica and pore water build-up of silicic acid in marine sediments. Marine Chemistry, 73,

673   333-352.

674   Frings, P.J., Clymans, W., Jeppesen, E., Lauridsen, T.L., Struyf, E., and Conley, D.J. (2014) Lack of

675   steady-state in the global biogeochemical Si cycle: emerging evidence from lake Si sequestration.

676   Biogeochemistry, 117, 255-277.

677   Gaillou, E., Delaunay, A., Rondeau, B., Bouhnik-le-Coz, M., Fritsch, E., Cornen, G., and Monnier, C.

678   (2008) The geochemistry of gem opals as evidence of their origin. Ore Geology Reviews, 34,

679   113-126.

680   Gehlen, M., Beck, L., Calas, G., Flank, A.M., Van Bennekom, A.J., and Van Beusekom, J.E.E. (2002)

681   Unraveling the atomic structure of biogenic silica: Evidence of the structural association of Al

682   and Si in diatom frustules. Geochimica et Cosmochimica Acta, 66, 1601-1609.

683   Gehlen, M., Heinze, C., Maier-Reimer, E., and Measures, C.I. (2003) Coupled Al-Si geochemistry in

684   an ocean general circulation model: A tool for the validation of oceanic dust deposition fields?

685   Global Biogeochemical Cycles, 17.

686   Guthrie, G.D., Bish, D.L., and Reynolds, R.C. (1995) Modeling the X-ray diffraction pattern of

687   opal-CT. American Mineralogist, 80, 869-872.

688   Hydes, D. J. (1989) Seasonal-variation in dissolved aluminum concentrations in coastal waters and

689   biological limitation of the export of the riverine input of aluminum to the deep-sea. Continental

690   Shelf Research, 9, 919-929.

691   Horton, D., Director, M., and Limited, O.H. (2002) Australian sedimentary opal: why is Australia

692   unique? The Australian Gemmologist, 21.

693   Houston, J.R., Herberg, J.L., Maxwell, R.S., and Carroll, S.A. (2008) Association of dissolved

694   aluminum with silica: Connecting molecular structure to surface reactivity using NMR.

695   Geochimica et Cosmochimica Acta, 72, 3326-3337.

696   Ibrahim, S.S., and Selim, A.Q. (2010) Producing a microporous diatomite by a simple classification-c

697   alcination process. The Journal of ORE DRESSING, 12, 25-33.

698   Ingall, E.D., Diaz, J.M., Longo, A.F., Oakes, M., Finney, L., Vogt, S., Lai, B., Yager, P.L., Twining,

699   B.S., and Brandes, J.A. (2013) Role of biogenic silica in the removal of iron from the Antarctic

700   seas. Nature Communications, 4, 1-6.

701   Jin, J., Ouyang, J., and Yang, H.M. (2014) One-step synthesis of highly ordered Pt/MCM-41 from

702   natural diatomite and the superior capacity in hydrogen storage. Applied Clay Science, 99,

703   246-253.

704   Jones, J.B., and Segnit, E.R. (1971) The nature of opal I. nomenclature and constituent phases. Journal

705   of the Geological Society of Australia, 18, 57-68.

706   Koning, E., Gehlen, M., Flank, A.M., Calas, G., and Epping, E. (2007) Rapid post-mortem

707   incorporation of aluminum in diatom frustules: Evidence from chemical and structural analyses.

708   Marine Chemistry, 106, 208-222.

709   Koshikawa, M. K., Sugiyama M., and Hori. T. (2002) Seasonal variation of dissolved aluminum

710   concentration in harmonic-type Lake Biwa, Japan. Limnology, 31, 1-9.

711   Kröger, N., Deutzmann, R., and Sumper, M. (1999) Polycationic peptides from diatom biosilica that

712   direct silica nanosphere formation. Science, 286, 1129–32.

713   Kröger, N., and Poulsen, N. (2008) Diatoms-from cell wall biogenesis to nanotechnology. Annual

714   Review of Genetics, 42, 83-107.

27

715 Lazaro, A., Sato, K., Brouwers, H.J.H., and Geus, J.W. (2018) Pore structure development of silica

716 particles below the isoelectric point. Microporous and Mesoporous Materials, 267, 257-264.

717 Liu, D., Yu, W.B., Deng, L.L., Yuan, W.W., Ma, L.Y., Yuan, P., Du, P.X., and He, H.P. (2016) Possible

718 mechanism of structural incorporation of Al into diatomite during the deposition process I. Via a

719 condensation reaction of hydroxyl groups. Journal of Colloid and Interface Science, 461, 64-68.

720 Liu, D., Yuan, P., Tan, D.Y., Liu, H.M., Fan, M.D., Yuan, A.H., Zhu, J.X., and He, H.P. (2010) Effects

721 of inherent/enhanced solid acidity and morphology of diatomite templates on the synthesis and

722 porosity of hierarchically porous carbon. Langmuir, 26, 18624-18627.

723 Liu, D., Yuan, P., Tan, D.Y., Liu, H.M., Wang, T., Fan, M.D., Zhu, J.X., and He, H.P. (2012) Facile

724 preparation of hierarchically porous carbon using diatomite as both template and catalyst and

725 methylene blue adsorption of carbon products. Journal of Colloid and Interface Science, 388,

726 176-184.

727 Losic, D., Mitchell, J.G., and Voelcker, N.H. (2009) Diatomaceous lessons in nanotechnology and

728 advanced materials. Advanced Materials, 21, 2947-2958.

729 Loucaides, S., Van Cappellen, P., Roubeix, V., Moriceau, B., and Ragueneau, O. (2012) Controls on

730 the recycling and preservation of biogenic silica from biomineralization to burial. Silicon, 4,

731 7-22.

732 Maher, S., Kumeria, T., Aw, M.S., and Losic, D. (2018) Diatom silica for biomedical applications:

733 Recent progress and advances. Advanced Healthcare Materials, 7.

734 Marchetti, A., Parker, M.S., Moccia, L.P., Lin, E.O., Arrieta, A.L., Ribalet, F., Murphy, M.E.P.,

735 Maldonado, M.T., and Armbrust, E.V. (2009) Ferritin is used for iron storage in bloom-forming

736 marine pennate diatoms. Nature, 457, 467-470.

737 Martin, E., and Gaillou, E. (2018) Insight on gem opal formation in volcanic ash deposits from a

738 supereruption: A case study through oxygen and hydrogen isotopic composition of opals from

739 Lake Tecopa, California, USA. American Mineralogist, 103, 803-811.

740 Matteson, A., Tomanic, J.P., Herron, M.M., Allen, D.F., and Kenyon, W.E. (2000) NMR relaxation of

741 clay/brine mixtures. SPE Reservoir Evaluation & Engineering, 3, 408-413.

742   Michalopoulos, P., and Aller, R.C. (1995) Rapid clay mineral formation in amazon delta sediment -

743   reverse weathering and oceanic elemental cycles. Science, 270, 614-617.

744   Montgomery, S.L., and Morea, M.F. (2001) Antelope shale (Monterey Formation), Buena Vista Hills

745   field: Advanced reservoir characterization to evaluate CO_2 injection for enhanced oil recovery.

746   AAPG Bulletin, 85, 561-585.

747   Moran, S.B., and Moore, R.M. (1988) Evidence from mesocosm studies for biological removal of

748   dissolved aluminium from sea water. Nature, 335, 706-708.

749   Niwa, M., Katada, N., and Okumura, K. (2010) Characterization and Design of Zeolite Catalysts:

750   Solid Acidity, Shape Selectivity and Loading Properties, 71p. Berlin, Heidelberg, Germany.

751   Presti, M., and Michalopoulos, P. (2008) Estimating the contribution of the authigenic mineral

752   component to the long-term reactive silica accumulation on the western shelf of the Mississippi

753   River Delta. Continental Shelf Research, 28, 823-838.

754   Rondeau, B., Cenki-Tok, B., Fritsch, E., Mazzero, F., Gauthier, J.P., Bodeur, Y., Bekele, E., Gaillou, E.,

755   and Ayalew, D. (2012) Geochemical and petrological characterization of gem opals from

756   WegelTena, Wollo, Ethiopia: opal formation in an Oligocene soil. Geochemistry: Exploration,

757   Environment, Analysis, 12, 93-104.

758   Shi, J.Y., Yao, Q.Z., Li, X.M., Zhou, G.T., and Fu, S.Q. (2012) Controlled morphogenesis of

759   amorphous silica and its relevance to biosilicification. American Mineralogist, 97, 1381-1393.

760   Shukla, S.K., and Mohan, R. (2012) The contribution of diatoms to worldwide crude oil deposits. The

761   Science of Algal Fuels, 355-382.

762   Snelling, A. A. (1995) The whale fossil in diatomite, Lompoc, California. Creation Ex Nihilo

763   Technical Journal, 9, 244-258.

764   Strand, S., Hjuler, M.L., Torsvik, R., Pedersen, J.I., Madland, M.V., and Austad, T. (2007) Wettability

765   of chalk: impact of silica, clay content and mechanical properties. Petroleum Geoscience, 13,

766   69-80.

767   Treguer, P., Bowler, C., Moriceau, B., Dutkiewicz, S., Gehlen, M., Aumont, O., Bittner, L., Dugdale,

768   R., Finkel, Z., Iudicone, D., and others. (2018) Influence of diatom diversity on the ocean

769   biological carbon pump. Nature Geoscience, 11, 27-37.

770   Treguer, P.J., and De La Rocha, C.L. (2013) The world ocean silica cycle. Annual Review of Marine

771   Science, 5, 477-501.

772   Turov, V.V., and Leboda, R. (1999) Application of ^{1}H NMR spectroscopy method for determination of

773   characteristics of thin layers of water adsorbed on the surface of dispersed and porous adsorbents.

774   Advances in Colloid and Interface Science, 79, 173-211.

775   Ushizaka, S., Sugie, K., Yamada, M., Kasahara, M., and Kuma, K. (2008) Significance of Mn and Fe

776   for growth of coastal marine diatom Thalassiosira weissflogii. Fisheries Science, 74, 1137-1145.

777   van Hulten, M.M.P., Sterl, A., Middag, R., de Baar, H.J.W., Gehlen, M., Dutay, J.C., and Tagliabue, A.

778   (2014) On the effects of circulation, sediment resuspension and biological incorporation by

779   diatoms in an ocean model of aluminium. Biogeosciences, 11, 3757-3779.

780   Wang, M., Xiang, Y.B., Zhang, G.L., Song, J.M., Cai, D.Q., and Wu, Z.Y. (2013) A facile approach to

781   improve the quality of diatomite as sulfuric acid catalyst support. Applied Catalysis A-General,

782   466, 185-189.

783   Webb, J.A., and Finlayson, B.L. (1987) Incorporation of Al, Mg, and water in opal-A-evidence from

784   speleothems. American Mineralogist, 72, 1204-1210.

785   Wysokowski, M., Jesionowski, T., and Ehrlich, H. (2018) Biosilica as a source for inspiration in

786   biological materials science. American Mineralogist, 103, 665-691.

787   Yuan, P., Wu, D.Q., Chen, Z., Chen, Z.W., Lin, Z.Y., Diao, G.Y., and Peng, J.L. (2001) ^{1}H MAS NMR

788   spectra of hydroxyl species on diatomite surface. Chinese Science Bulletin, 46, 1118-1121.

789   Yuan, P., Wu, D.Q., He, H.P., and Lin, Z.Y. (2004) The hydroxyl species and acid sites on diatomite

790   surface: a combined IR and Raman study. Applied Surface Science, 227, 30-39.

791   Yuan, W.W., Yuan, P., Liu, D., Yu, W.B., Laipan, M.W., Deng, L.L., and Chen, F.R. (2016) In situ

792   hydrothermal synthesis of a novel hierarchically porous TS-1/modified-diatomite composite for

793   methylene blue (MB) removal by the synergistic effect of adsorption and photocatalysis. Journal

794   of Colloid and Interface Science, 462, 191-199.

795   Zhang, S.Q., Wang W.M., Sun G., Wang P.J., Gao Y.F., Yang T., Chen C.Y., and Wang Y. Q. (2019).

796   Late Cenozoic palynofloras revealing significant environment and climate changes in Changbai

797   Mountain area, NE China. Review of Palaeobotany and Palynology, 261, 1-10.

798

List of Figure Captions

799

800 **Figure 1.** Schematic representation of the steps of conducting the FIB thinning treatment.

801 The microscopic images are from the characterization by the FE-SEM, which was used to

802 monitor the morphological changes of the intermediate products during FIB thinning. The

803 frustule of diatom of *Melosira granulate* (Ehr.) was from S-Dt. "Slice" refers to the final

804 thin-layered sample (with thickness of approximately 80 nm) of a fragment of the frustule

805 produced from FIB treatment, which was used for further TEM characterization.

806 **Figure 2.** Powder XRD patterns of the diatomite samples. (a) C-Dt; (b) S-Dt; (c) L-Dt

807 **Figure 3.** Morphology a frustule from C-Dt and the elemental distribution in it. (a) SEM

808 image of a diatom frustule of the genus *Coscinodiscus Ehrenberg.* The inset is the image

809 of the pores at the edge of the frustule. (b) The scheme of the upper epivalve of the

810 frustule; a fragment of it was further sliced by using FIB thinning. (c) The FESEM image

811 of a sliced fragment of the frustule, produced from FIB thinning. (d) The EDS mapping

812 pictures showing the elemental distribution results of Area-A that is indicated in Fig. 3c.

813 "BF" refers to bright field. The black-coloured background in the EDS mapping images

814 represents void.

815 **Figure 4.** TEM images of the sliced fragment of the frustule in C-Dt. (a) TEM image of a

816 fraction of the sliced fragment of the frustule shown in Fig. 3c. (b) TEM image of the

817 areas outlined in Fig. 4a, where some local areas used for EDS mapping characterization

818 are marked. (c) The EDS spectra of selected locations, Place-6, Place-7 and Place-8,

819 which are shown in Fig. 4b.

820

821 **Figure 5.** Morphology and elemental distribution of a frustule from S-Dt. (a) SEM image

822 of the same diatom frustule of the genus *Melosira granulate* (Ehr.) *Ralfs* shown in Fig. 1.

823 (b) The EDS mapping results showing the elemental distribution of Area-I (indicated in

824 Fig. 5a). (c) The EDS mapping results showing the elemental distribution of Area-II

825 (indicated in Fig. 5a).

826   **Figure 6.** TEM images of the sliced fragment of the frustule in C-Dt. (a) TEM image of a

827   fraction of the sliced fragment of the frustule shown as Fig. 5a. (b) TEM image of a

828   partial area of the zone shown in Fig. 6a, in which some places used for EDS mapping

829   are marked. (c) TEM image of another partial area of the zone shown in Fig. 6a.

830   **Figure 7.** Morphology a frustule in L-Dt and the elemental distribution in it. (a) SEM

831   image of a diatom frustule of genus *Melosira granulate* (Ehr.) *Ralfs*. (b) The FESEM

832   image of a sliced fragment of the frustule, produced from FIB thinning. (c) The TEM

833   image of the sliced fragment shown in (b). (d) The EDS mapping pictures showing the

834   elemental distribution results of the selected area shown in (c). (e) High-resolution (HR)

835   TEM images of the selected area shown in (c), where some places used for EDS mapping

836   characterization are marked. The inset at the right corner of (e) is the HRTEM image of

837   the rectangular area shown in (e).

838   **Figure 8.** TEM images of selected locations in the sliced fragments of the frustule from

839   C-Dt. (a) layered images of High-angle annular dark-field scanning transmission electron

840   microscopy (HAADF-STEM) and Al EDS mapping (yellow dots) of the selected location

841   (Place-1 in Fig. 4b) in the sliced fragment. (b) HRTEM images of the selected area shown

842   in (a). The insets at the right and left bottom of (b) are the SAED pattern and

843   high-resolution (HR) TEM image of the rectangular area shown in (b), respectively. (c)

844   layered images of HAADF-STEM and Al EDS mapping (yellow dots) of the selected

845   location (Place-6 in Fig. 4b). (d) HRTEM image of the square area in (c) and its SAED

846   (the inset at the left corner).

847

848

849

850

Supporting Information

851

Results of the zeta potential and the isoelectric point (pH$_{IEP}$) measurement

852

853   Zeta potential measurements were conducted on a Zetasizer Nano-ZS90 type

854   zeta-porential analyzer (Malven, Britain). A suspersion with solid/liquid ratio of 40

855   mg/1L was prepared by putting diatomite powder into ultrapure water (18.25 MΩ·cm).

856   The dispersion was stirred for 10 min and then was treated by centrifugation with

857   centrifugation speed of 2500 r/min for 1 min. The obtained supernatant was used for the

858   zeta potential measurement. The measurements were repeated for 3 times.

859   Two diatomite samples were used for the zeta potential measurement. One is the

860   C-Dt sample which was treated by sedimentation method. The method is as follows. 150

861   g raw C-Dt was dispersed in a 5 L graduated cylinder with ultra-pure water to height of

862   35 cm and then vigorously stirred for 30 min. The dispersion was withdrawn by

863   siphoning after the accurate sedimentation time. The sedimentation time (t, s) needed was

864   determined by the following equation according to the Stokes' law. The sedimentation

865   process was performed for 2 times. The purified diatomite (denoted C-Dt$_P$) was dried at

866   105°C.

867   The other diatomite sample is the C-Dt sample underwent acid washing and

868   calcination treatment. The procedures are as follows. 2 M HCl solution was used to treat

869   the diatomite sample with a ratio of HCl/diatomite of 15ml/1g, and the suspension was

870   kept stirring under 105°C water bath for 4 h. The resulting solid product was obtained by

871   repeated centrifugation and washing until free of Cl$^-$ (tested by AgNO$_3$). After drying at

872   105°C, the acid-treated diatomite sample was then calcined at 450°C in muffle oven for 2

873   h. The product was denoted C-Dt$_A$.

874   Figure S1 shows that, at the whole pH range, C-Dt$_P$ shows negative potential (-25 −

875   -50 mV), indicating it possesses constant negative charge. However, C-Dt$_A$ exhibits an

876   isoelectric point of 1.9, i.e., the zeta potential at this pH value is zero. Since the acid

877   washing combined calcination is able to remove the impurity phase of diatomite whereas

878   sedimentation treatment is not, the different performance between $C\text{-}Dt_P$ and $C\text{-}Dt_A$

879   indicates that the impurity of diatomite strongly affect the surface charge of diatomite.

880

881

882
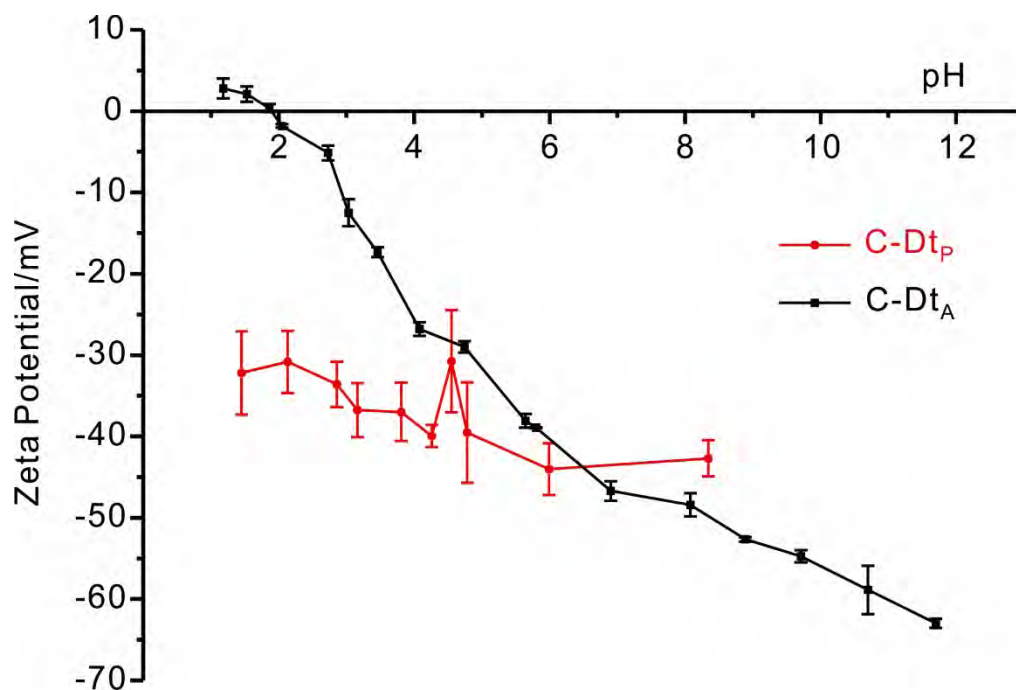
883   **Figure S1.** Zeta potential measurement results of diatomite $C\text{-}Dt_P$ and $C\text{-}Dt_A$

884

885

886

887 **Table 1.** The contents of the minor elements in the frustules from different diatomite samples, represented by the atomic ratio of the minor
888 element to silicon (Si).

Sample	Region / Places	Al/Si	Fe/Si	Mg/Si	Ca/Si	K/Si	Zn/Si	Sample	Region / Places	Al/Si	Fe/Si	Mg/Si	Ca/Si	K/Si	Zn/Si
C-Dt	Area-A	0.0230	0.0047	0.0004	0.0013	0.0026	0.0030		Place-3	0.0012	0.0009	0.0012	0.0003	0.0003	0.0003
	Area-B	0.0052	0.0017	0.0002	0.0002	0.0007	0.0007		Place-9	0.0016	0.0008	0.0013	0.0003	0.0005	0.0002
	Place-2	0.0012	0.0009	0.0009	0.0003	0.0003	0.0006		Place-12*	0.0019	0.0014	0.0027	0.0011	0.0008	0.0005
	Place-8	0.0064	0.0019	0.0013	0.0006	0.0006	0.0010	Internal	Place-13*	0.0012	0.0009	0.0009	0.0003	-	0.0003
	Place-9*	0.0059	0.0029	0.0032	0.0018	0.0026	0.0015	structure	Place-14*	0.0025	0.0011	0.0022	0.0008	0.0011	0.0003
	Place-10*	0.0037	0.0046	0.0043	0.0015	0.0025	0.0009		Place-15*	0.0028	0.0012	0.0021	0.0005	0.0009	0.0007
Internal	Place-11*	0.0028	0.0003	0.0016	0.0003	0.0006	0.0009		Place-16*	0.0028	0.0009	0.0018	0.0012	0.0006	0.0006
structure	Place-12*	0.0059	0.0028	0.0059	0.0019	0.0028	0.0009		Place-17*	0.0009	0.0006	0.0012	0.0003	0.0003	0.0003
	Place-13*	0.0019	0.0026	0.0016	0.0006	0.0006	0.0003		Place-18*	0.0041	0.0009	0.0035	0.0015	0.0009	0.0012
	Place-14*	0.0065	0.0065	0.0028	0.0028	0.0041	0.0017		Place-1	0.0852	0.0385	0.0385	0.0055	0.0192	0.0110
	Place-15*	0.0036	0.0044	0.0039	0.0022	0.0017	0.0019		Place-2	0.0452	0.0190	0.0167	0.0131	0.0143	0.0131
	Place-16*	0.0041	0.0054	0.0017	0.0012	0.0041	0.0029		Place-4	0.0452	0.0040	-	0.0062	0.0022	0.0058
	Place-17*	0.0062	0.0036	0.0033	0.0026	0.0029	0.0020		Place-7	0.0708	0.0230	0.0529	0.0179	0.0136	0.0281
	Place-18*	0.0019	0.0013	0.0016	0.0006	0.0010	0.0006	S-Dt / Subsurface	Place-8	0.0386	0.0346	0.0427	0.0346	0.0183	0.0122
	Place-3	0.0117	0.0028	0.0011	0.0021	0.0028	0.0018		Place-10	0.0352	0.0018	0.0015	0.0066	0.0022	0.0011
	Place-4	0.0167	0.0130	0.0107	0.0047	0.0070	0.0043		Place-19*	0.0255	0.0255	-	0.0179	0.0306	0.0077
	Place-7	0.0718	0.0438	0.0630	0.0298	0.0385	0.0753		Place-20*	0.0406	0.0031	0.0058	0.0062	0.0018	0.0076
	Place-19*	0.0104	0.0117	-	0.0097	0.0110	0.0013		Place-21*	0.0717	0.0358	-	0.0179	0.0430	0.0287
Subsurface	Place-20*	0.0231	0.0154	0.0035	0.0049	0.0115	0.0056		Place-22*	0.0488	0.0220	0.0146	0.0244	0.0756	0.0098
	Place-21*	0.0216	0.0043	0.0138	-	0.0062	0.0007		Place-5	0.0788	0.0190	-	0.0190	0.0326	0.0245
	Place-22*	0.0787	0.0132	0.0007	0.0033	0.0081	0.0011	Surface	Place-6	0.1208	0.0340	-	0.0453	0.0453	0.2189
	Place-23*	0.0246	0.0057	-	0.0038	0.0035	0.0035		Place-11	0.0923	0.0564	-	0.0308	0.0615	0.0205
	Place-24*	0.0280	0.0268	0.0052	0.0128	0.0198	0.0041		Place-23*	0.0745	0.0239	-	0.0266	0.0452	0.0479
	Place-1	0.3907	0.0817	0.0269	0.0047	0.0610	0.0026		Place-24*	0.1207	0.1010	-	0.0591	0.0739	0.0690
	Place-5	0.2296	0.2074	0.0148	0.1185	0.1111	0.1407	Internal	Place-1	0.0016	0.0010	0.0016	0.0006	0.0006	0.0006
	Place-6	0.4777	0.1403	0.0302	0.0220	0.0378	0.0019	structure	Place-2	0.0050	0.0003	0.0012	0.0003	0.0006	0.0003
	Place-25*	0.2357	0.1857	0.1429	0.1500	0.1714	0.0571		Place-3	0.0019	0.0006	0.0013	0.0006	0.0006	0.0003
Surface	Place-26*	0.3083	0.1889	0.1833	0.0861	0.0917	0.1083		Place-8	0.0019	0.0006	0.0015	0.0006	0.0006	0.0003
	Place-27*	0.3782	1.4706	0.3782	0.2689	0.3445	0.5630	Subsurface	Place-4	0.0139	0.0026	0.0110	-	0.0048	0.0359
	Place-28*	0.3898	0.0064	0.1335	0.0254	0.1038	0.0911	L-Dt	Place-5	0.0063	0.0036	-	0.0040	0.0083	0.0008
	Place-29*	0.2242	0.0266	0.0340	0.0100	0.0209	0.0048		Place-9	0.0261	0.0112	0.0036	0.0058	0.0063	0.0031
	Place-30*	0.1186	0.0499	-	0.0355	0.0532	0.0366	Surface	Place-6	0.0322	0.0302	0.1429	0.0262	0.0342	0.0040
S-Dt	Area-I	0.0047	0.0021	-	0.0011	0.0016	0.0005		Place-7	0.1004	0.0961	0.0786	0.0699	0.0699	0.1878
	Area-II	0.0035	0.0010	-	0.0005	0.0015	-		Place-10	0.0950	0.0588	-	0.0407	0.0724	0.0543

889 * These data are from the measurements on the frustules from the same diatomite sample, but not from the frustules whose images are shown in the manuscript.
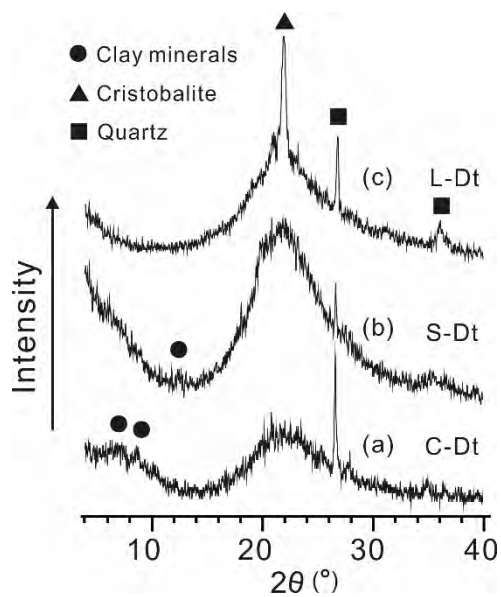
890

Figure 1
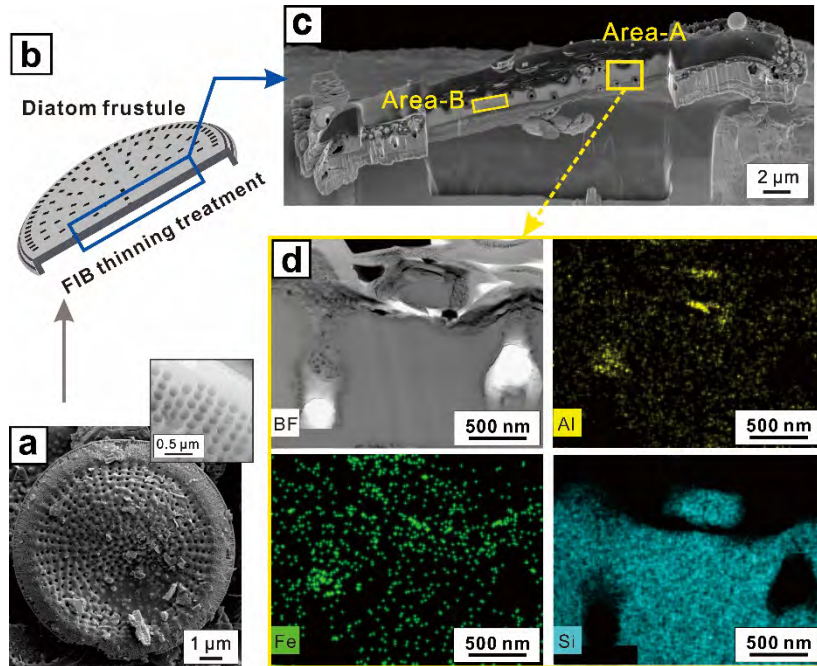
891
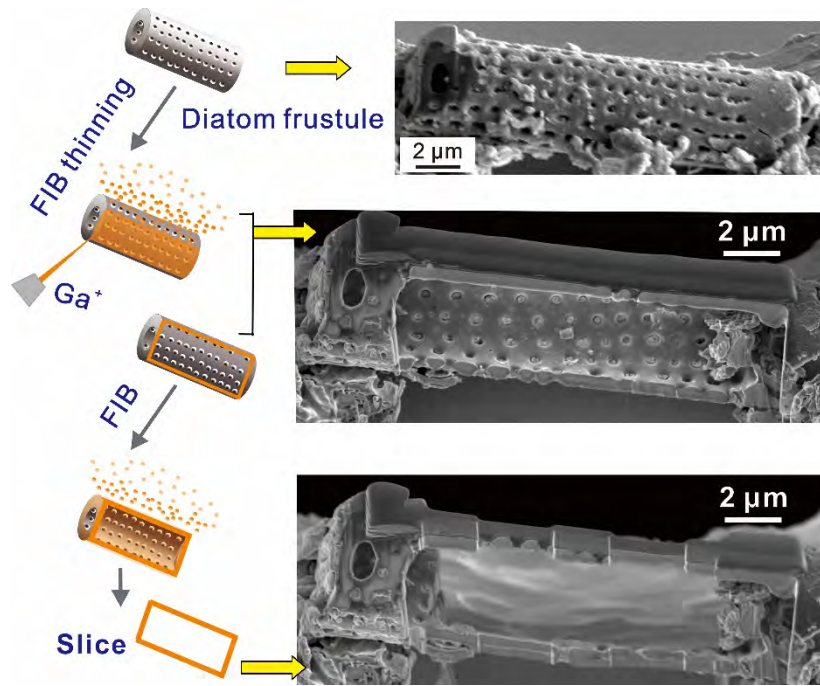
892

893

894

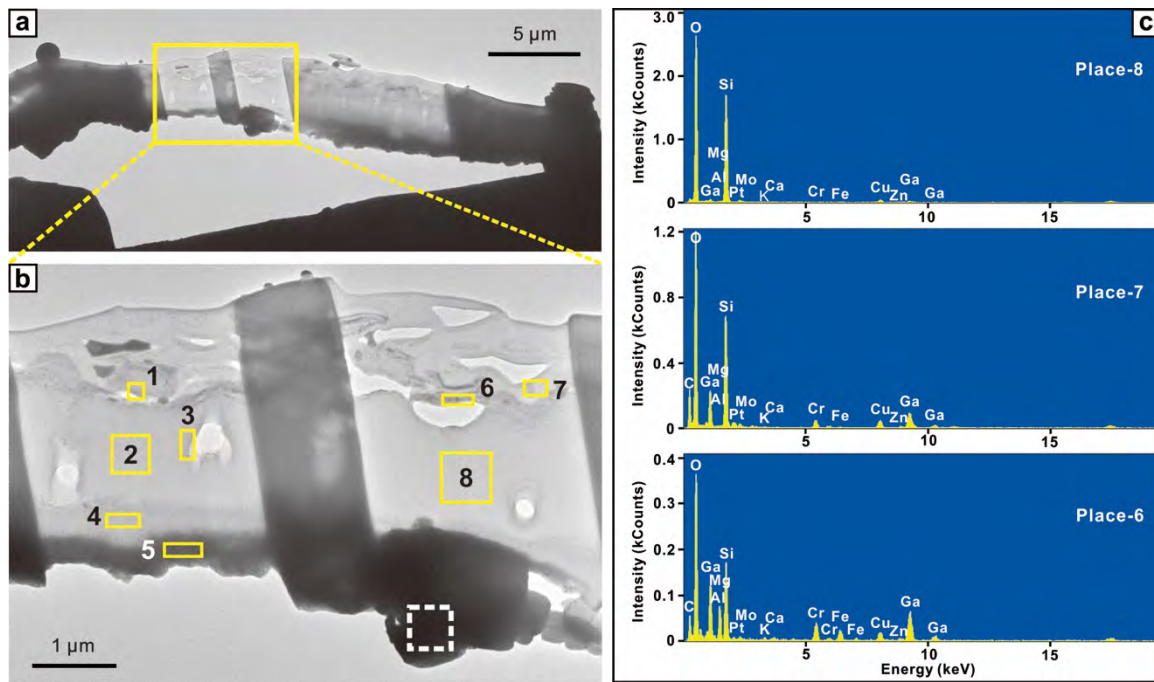895 **Figure 2**

896

897

898

899

900

901

902

Figure 3

903

904

905

Figure 4

906

907

908

909

Figure 5

910

911

912

913 **Figure 6**

914
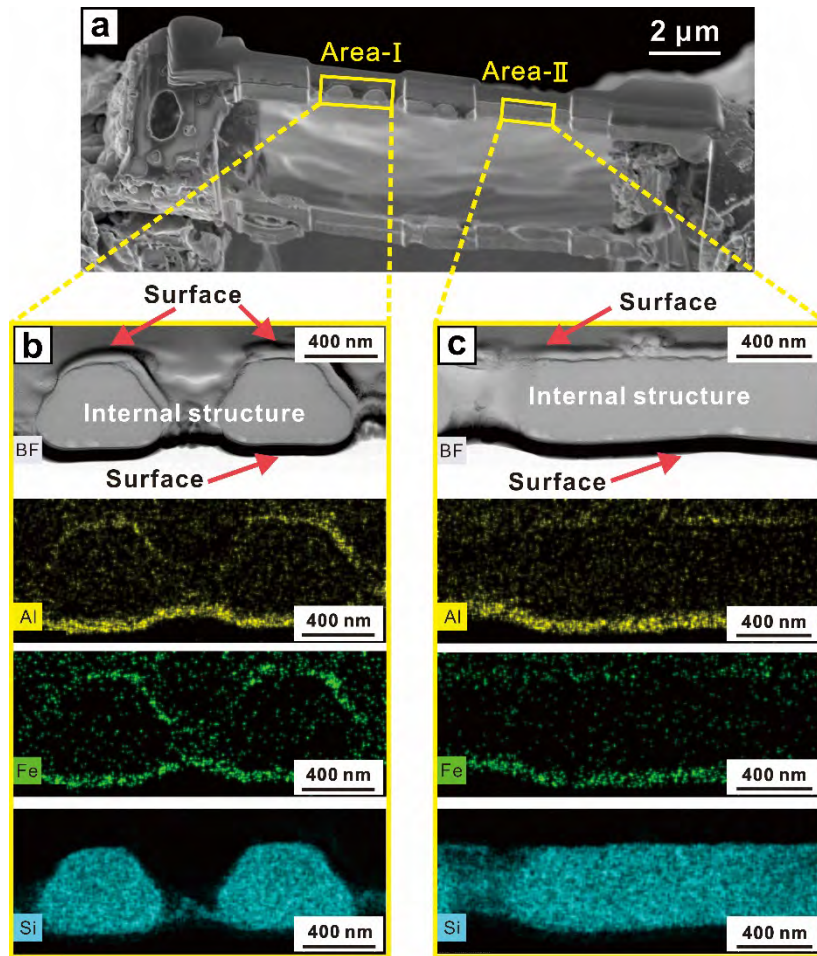
915

916 **Figure 7**
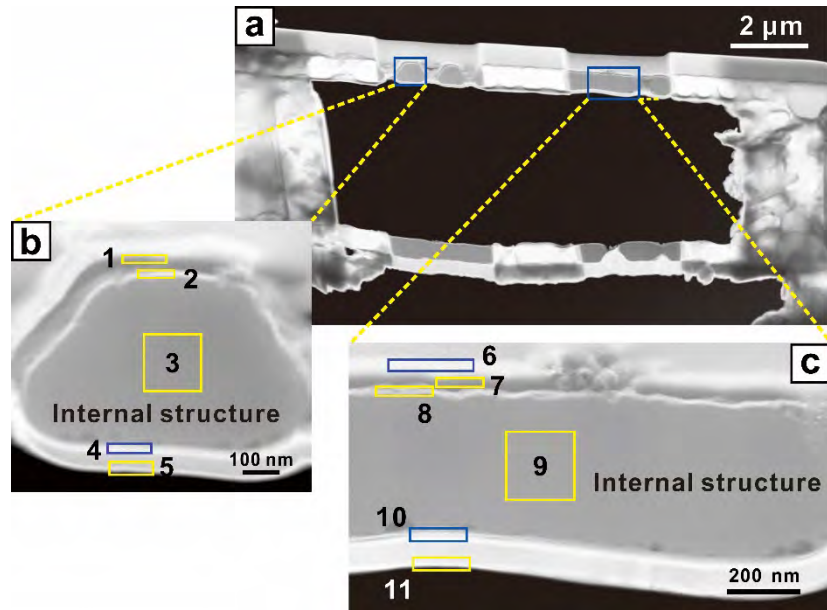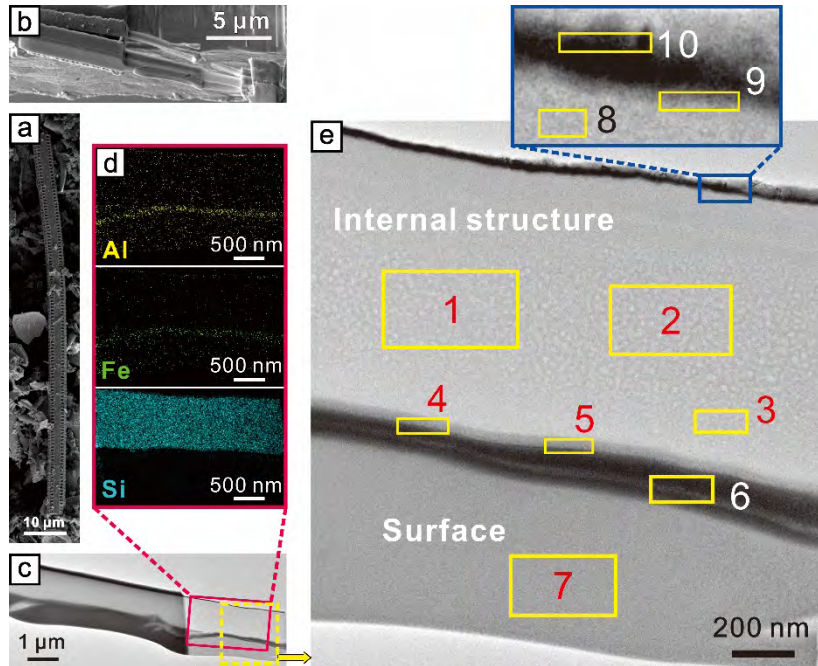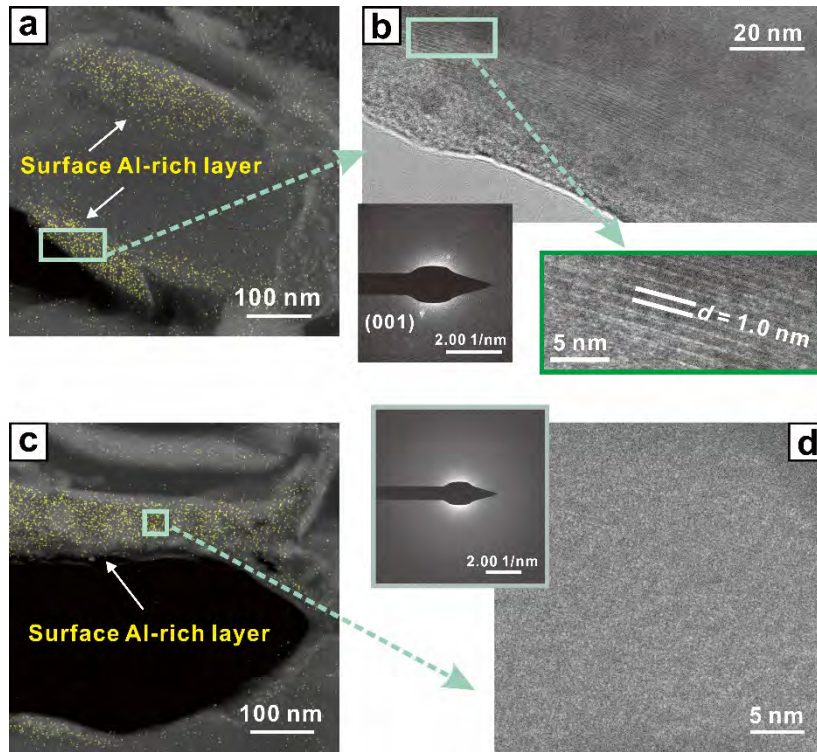
917

918
919

920

921   **Figure 8**

922

923

44